ACS APPLIED MATERIALS & INTERFACES

Research Article

www.acsami.org

Size-Dependent Property and Cell Labeling of Semiconducting Polymer Dots

Kai Sun,[†] Haobin Chen,[†] Lei Wang,[†] Shengyan Yin,[†] Haiyu Wang,[†] Gaixia Xu,[‡] Danni Chen,[‡] Xuanjun Zhang,[§] Changfeng Wu,*[,†] and Weiping Qin*[,†]

[†]State Key Laboratory on Integrated Optoelectronics, College of Electronic Science and Engineering, Jilin University, Changchun, Jilin 130012, China

[‡]Key Laboratory of Optoelectronic Devices and Systems of Ministry of Education and Guangdong Province, Shenzhen University, Shenzhen 518060, China

[§]Division of Molecular Surface Physics & Nanoscience, Department of Physics, Chemistry, and Biology, Linköping University, Linköping 58183, Sweden

Supporting Information

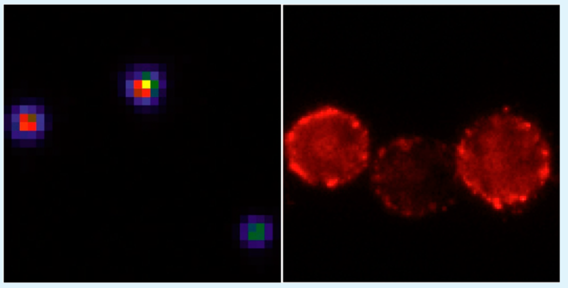

ABSTRACT: Semiconducting polymer dots (Pdots) represent a new class of fluorescent nanoparticles for biological applications. In this study, we investigated their size-dependent fluorescence and cellular labeling properties. We demonstrate that the polymer conformation in solution phase largely affects the polymer folding and packing during the nanoparticle preparation process, resulting in solution-phase control over the fluorescence properties of semiconducting polymer nanoparticles. The resulting Pdots exhibit apparent size dependent absorption and emission, a characteristic feature of different chain packing behaviors due to the preparation conditions. Single-particle fluorescence imaging was employed to perform a side-by-side comparison on the Pdot brightness, indicating a quadratic dependence of single-particle brightness on particle size. Upon introducing a positively charged dye Nile blue, all the three type of Pdots were quenched very efficiently ($K_{sv} > 1 \times 10^7$ M^{-1}) in an applied quenching process at low dye concentrations, but exhibit apparent difference in quenching efficiency with increasing dye concentration. Furthermore, Pdots of different sizes were used for cell uptake and cellular labeling involving biotin–streptavidin interactions. Fluorescence imaging together with flow cytometry studies clearly showed size dependent labeling brightness. Small-sized Pdots appear to be more effective for immunolabeling of cell surface, whereas medium-sized Pdots exhibit the highest uptake efficiency. This study provides a concrete guidance for selecting appropriate particle size for biological imaging and sensing applications.

KEYWORDS: *conjugated polymer, nanoparticle, fluorescence, spectroscopy, single-particle imaging, quenching*

■ INTRODUCTION

Fluorescent semiconducting polymer dots (Pdots) have recently attracted a great deal of attention because of their superior characteristics as fluorescent labels. Salient features include their extraordinary brightness, fast emission rate, excellent photostability, nonblinking, and nontoxic features.[1−5] The Pdots are made primarily from hydrophobic polymers and their formation results from collapse of polymer chains due to sudden decrease in solvent hydrophobicity.[1] Consequently, the internal structures of the Pdots are highly complex because of morphological effects, such as chain–chain packing, conformational defects, aggregation, bending and kinking of the polymer chain, and so forth. The polymer chain morphology and packing behavior significantly affect the optical properties of semiconducting polymers, as confirmed by a number of studies indicating that the emission color and quantum yield of solution-processed conjugated polymer thin films are highly dependent on various factors and processing steps such as choice of solvent, polymer concentration, and thermal annealing.[6−8] The emission mechanism of conjugated polymers in solid state (dense packed films and nanoparticles) is primarily due to singlet excitons that are trapped in dilute, low-energy chain segments (red sites). The "red sites" are attributed to the local tightly packed regions having relatively close chain–chain contacts, where the chain–chain electronic interactions lower the energy.[9] The absorption, however, originates predominately from more plentiful high-energy segments (blue sites), which can transfer energy to the red sites with very high efficiency (approaching unit in many cases).[10] As inorganic quantum dots exhibit pronounced variations in band gap because of the quantum size effect, the optical properties of conjugated polymer nanoparticles can also

Received: May 7, 2014
Accepted: June 16, 2014
Published: June 16, 2014

be tuned by their particle size, in particular the chemical alteration of the π-conjugated molecular structures and their intermolecular interactions.[11]

Fluorescent conjugated polymers have also been extensively used for biosensor applications. In this aspect, considerable interest has been focused on water-soluble conjugated polymers (conjugated polyelectrolytes), which exhibit amplified quenching (superquenching) when interacting with ionic species such as organic dyes, metal nanoparticles, and biopolymers.[12−19] The high quenching sensitivity was attributed to a combined effect of efficient energy/exciton migration with strong association between the polymer and the quenchers. In comparison with single polymer chain, the quenching in aggregated polymer chains can be greatly enhanced because interchain exciton migration occurs and the quenching volume of single quencher increases.[16] Pdots represent a typical multichromophoric system with densely packed polymer chains and 3D exciton migration pathways, as confirmed by efficient energy transfer in fluorescent dye-doped Pdots.[20,21] By selecting dye molecules of certain sensing functions, novel dye-doped Pdots have been developed for ratiometric determination of important cellular parameters such as oxygen, pH, temperature, and reactive oxygen species.[22−25] Very recently, Pdots as nanoparticle donors were employed to develop FRET based molecular beacons for detection of tumor marker such as carcinoembryonic antigen (CEA).[26] These results indicate that Pdots are promising platforms for quenching based sensor applications.

For fluorescence quenching induced by surface acceptors, the physical size of Pdots is deemed to affect the quenching efficiency as well as the sensor sensitivity because the quenchers (large biomolecules in particular) may only be able to approach certain sites on particle surface (not the interior of Pdots). In addition, the per-particle brightness of Pdots is also dependent on the particle size, but the brightness-size relationship has not been experimentally explored. Selection of appropriate particle size is particularly important for single-particle based sensors,[27] as one has to play a trade-off between the quenching sensitivity and signal level determined by single-particle brightness. It has been demonstrated that fluorescent Pdots are efficient probes for cellular recognition, imaging and drug delivery.[2,4] It is essential to understand the effect of particle size on cellular uptake and labeling to enable rational design of the Pdot-based agents. As a result of these issues, investigation of the size-dependent property and performance of Pdots remains an important subject for their widespread sensor and imaging applications.

In this paper, we attempt to prepare Pdots with relatively controlled size and explore the size effect on their fluorescence and cell labeling applications. A series of Pdots from small (~16 nm) to large particle size (~59 nm) were prepared by a two-step reprecipitation method. The resulting Pdots exhibit apparent size dependent absorption and emission, a characteristic feature of different chain packing behaviors due to the preparation conditions. We employed single-particle fluorescence imaging to perform a side-by-side comparison on the Pdot brightness, revealing a quadratic dependence of the per-particle brightness on the particle size. We performed fluorescence imaging and flow cytometry to investigate cellular uptake and cell-surface labeling using the Pdot-bioconjugates, which indicate apparent difference in cell labeling brightness upon their size change.

■ EXPERIMENTAL SECTION

Materials. The semiconducting polymer used in this study is polyphenylenevinylene derivative poly[2-methoxy-5-(2-ethylhexyloxy)-1,4-(1-cyanovinylene-1,4-phenylene)] (CN-PPV, average molecular weight: 235,000, polydispersity: 8.0). The polymer was purchased from American Dye Source, Inc. (Quebec, Canada). The functional polymer poly(styrene-*co*-maleic anhydride) (PSMA, cumene terminated, average MW ≈ 1700, styrene content 68%), fluorescent dye Nile blue (dye content 95%) and the solvent tetrahydrofuran (THF, anhydrous, ≥99.9%) were purchased from Sigma-Aldrich. The solvent ethanol (analytical reagent, ≥99.7%) was purchased from Beijing Chemical Works (Beijing, China). All chemicals were used without further purification and all experiments were performed at room temperature unless indicated otherwise.

Preparation of Semiconducting Polymer Nanoparticles. Preparation of the aqueous dispersion of semiconducting polymer nanoparticles was performed using a two-step reprecipitation method modified from previous reports.[28,29] The semiconducting polymer CN-PPV and functional polymer PSMA were dissolved in THF by stirring overnight under inert atmosphere, respectively. The solutions were the filtered through a 0.7 μm glass fiber filter in order to remove any insoluble material. Then the solution of CN-PPV was mixed with the solution of PSMA to produce a solution mixture with a CN-PPV concentration of 1 mg/mL and a PSMA concentration of 0.2 mg/mL. In order to prepare Pdots of different size, the above solution was further diluted in solution mixtures of THF and water with water volume fraction of 0, 30, and 50%, respectively. The diluted solutions have a CN-PPV concentration of 50 μg/mL and a PSMA concentration of 10 μg/mL. A 5 mL quantity of the above solution was added quickly to 10 mL of Milli-Q water in a bath sonicator while sonicating the mixture. The sudden decrease in solvent quality results in nanoparticle formation. The suspension solution was filtered with a 0.2 μm membrane filter. The solvent THF was removed by nitrogen stripping, and the solution concentrated to 5 mL on a 90 °C hot plate followed by filtration through a 0.2 μm filter. The Pdot dispersions were clear and stable for months without signs of aggregation.

The fluorescent dye, Nile blue (5 mg), was dissolved in anhydrous ethanol to make a 500 μg/mL solution. The precursor solution was further diluted to different concentrations (50 ppm, 10 ppm, 1 ppm, 0.1 ppm) using solvent ethanol. Varying amounts of dye solutions were mixed with aqueous suspensions of CN-PPV Pdots of different sizes, respectively. The final solution mixtures have a constant Pdot concentration of 6.7 ppm (absorbance of ~0.2) and dye fractions ranging from 0 to 8 wt % relative to the Pdots. The mixtures were agitated to form homogeneous solutions for spectroscopic characterizations.

Characterization Methods. The particle size and morphology of the CN-PPV Pdots were characterized by dynamic light scattering (DLS) and transmission electron microscopy (TEM). Dynamic light scattering was performed using a 1 cm disposable polystyrene cuvette at 25 °C with a Malvern Nano ZS instrument. Samples for TEM measurements were prepared by drop casting the Pdots dispersion onto copper grids. The samples were allowed to dry at room temperature, and then the TEM images were obtained using a Hitachi H-600 microscope operated at 120 kV. UV−vis absorption spectra were recorded with a Schimadzu UV-2550 scanning spectrophotometer using 1 cm glass cuvette. Fluorescence spectra were obtained using a Hitachi F-4500 fluorescence spectrophotometer.

Single-particle fluorescence imaging was performed by custom built Total Internal Reflection Fluorescence (TIRF) microscope. A 488 nm Sapphire laser beam (Coherent, USA) was directed into an inverted microscope (Olympus IX71, Japan) using steering optical lenses. The objective used for illumination and light collection was a 1.49 NA UAPON 100× TIRF objective (Olympus, Japan). Laser excitation power was measured at the nosepiece before the objective. Fluorescence signal was filtered by a 500 nm long pass filter and imaged on an Andor iXon3 frame transfer EMCCD (Andor Technology, UK). Fluorescent samples were diluted in Milli-Q water, dried under vacuum on cleaned glass coverslips, and imaged on the TIRF microscope. Fluorescence intensity emitted per frame for a given particle was estimated by integrating the CCD signal over the fluorescence spot.

Nanosecond fluorescence lifetime experiments were performed by the time-correlated single-photon counting (TCSPC) system under right-angle sample geometry. A 405 nm picosecond diode laser (Edinburgh Instruments EPL375, repetition rate 2 MHz) was used to excite the samples. The fluorescence was collected by a photomultiplier tube (Hamamatsu H5783p) connected to a TCSPC board (Becker & Hickel SPC-130). The combination of the detector and electronics results in an instrument response function (IRF) with a width of 300 ps (fwhm). Subpicosecond time-resolved emission were measured by the femtosecond fluorescence upconversion method. A mode-locked Ti:sapphire laser/amplifier system (Solstice, Spectra-Physics) was used. The output of the amplifier of 1.5-mJ pulse energy, 100 fs pulse width, at 800 nm wavelength is split into two equal parts; the second harmonic (400 nm) of one beam was focused in the sample as excitation. The resulted fluorescence was collected and focused onto a 1 mm thick BBO crystal with a cutting angle of 35 degree. The other part of the RGA output was sent into an optical delay line and served as the optical gate for the upconversion of the fluorescence. The generated sum frequency light was then collimated and focused into the entrance slit of a 300 mm monochromator. A UV-sensitive photomultiplier tube 1P28 (Hamamatsu) was used to detect the signal. The fwhm of instrument response function was about 400 fs.

Cell Culture and Nanoparticle Uptake. Breast cancer cell line MCF-7 cells were ordered from American Type Culture Collection (ATCC, Manassas, VA, USA). Cells were cultured in an atmosphere of air/CO_2 (95:5) at 37 °C, by using Dulbecco's modified Eagle Medium (DMEM) with 10% Fetal Bovine Serum (FBS), 50U/mL penicillin, and 50 μg/mL streptomycin. For cell uptake, 1.5×10^4 MCF-7 cells were plated onto a glass-bottomed microscope dishes and allowed to grow overnight. Sterile-filtered Pdot dispersions with different sizes was added to the cell culture media at the same weight concentration of ~25 ppm and allowed to incubate for 24 h. The cells were then washed with warm PBS buffer before viewing on a fluorescence microscope.

Pdot Bioconjugation and Immunofluorescent Labeling. We performed bionconjugation by utilizing the EDC-catalyzed reaction between carboxyl groups on Pdot surface and amine groups on biomolecules. Three types of Pdots were conjugated with strepatvidin, respectively, by the same protocol. In a typical bioconjugation reaction, 20 μL of poly(ethylene glycol) (5%w/v PEG, MW 3350) and 20 μL of concentrated HEPES buffer (1 M) were added to 1 mL of functionalized Pdot solution (50 μg/mL in Milli-Q water), resulting in a Pdot solution in 20 mM HEPES buffer with a pH of 7.4. Then, 60 μL of streptavidin (purchased from Sigma-Aldrich) was added to the solution and mixed well on a vortex. 20 μL of freshly prepared EDC solution (5 mg/mL in Milli-Q water) was added to the solution, and the above mixture was left on a rotary shaker for 4 h at room temperature. Finally, the resulting Pdot-streptavidin bioconjugates were separated from free biomolecules by gel filtration using Sephacryl HR-300 gel media. For labeling the surface marker EpCAM, MCF-7 cells were harvested from the culture flask, washed, centrifuged, and resuspended in a labeling buffer (1× PBS, 1% BSA). The MCF-7 cells were dispersed in 100 μL of labeling buffer in a 5 mL round-bottom tube, and sequentially incubated with a biotinylated primary anti-EpCAM (0.5 mg/mL) and Pdot-streptavidin. The Pdot-tagged cells were then fixed with 4% para-formaldehyde for 15 min, and then imaged on a fluorescence microscope and analyzed by flow cytometry.

Fluorescence Imaging and Flow Cytometry. Fluorescence imaging was performed on an inverted fluorescence microscope (Olympus IX71) with a 0.95 NA UPLSAPO 40× objective. The excitation light was provided with a Mercury Lamp, and filtered by a band-pass filter (Semrock FF01−445/45−25). Fluorescence signal was filtered by a band-pass filter (Semrock FF01−609/57−25), and imaged on an Andor iXon3 frame-transfer EMCCD (Andor Technology, UK). Flow cytometry was operated on a BD AccuriC6 flow cytometer (BD Biosciences, San Jose, CA, USA). A 488 nm laser was used for excitation and emission was collected through PE channel equipped with a 580/40 nm bandpass filter. Data were analyzed using the CFlow software (Accuri Cytometers).

RESULTS AND DISCUSSION

Nanoparticle Preparation and Size. Semiconducting polymer nanoparticles have been prepared by the reprecipitation method, in which rapid mixing of the polymer in THF solution with water result in nanoparticle formation driven by hydrophobic interactions.[28] A variety of semiconducting polymer nanoparticles have been demonstrated and their particle sizes can be generally controlled by adjusting the polymer concentration in the precursor solution.[1,2] However, this trend as well as the specific size distribution are dependent on the polymer species such as their molecular weight and backbone rigidity. Regarding the backbone rigidity of the polymer, rapid mixing of a dilute solution of polyfluorene (PFO, MW ~146 000) polymer in THF (400 ppm, 200 μL) with water (8 mL) under sonication results in the nanoparticles of ~50 nm diameter, and these nanoparticles can be well reproduced. Under the same preparation conditions, much smaller Pdots (~16 nm) were obtained for the CN-PPV polymer (MW ~235,000), indicating the apparent effect of polymer species (backbone rigidity) on particle size. The molecular weight for a given polymer also affects the particle size. For example, we can reproducibly prepare CN-PPV Pdots as small as ~10 nm by using a precursor polymer of low molecular weight (~15 000).[30] However, the smallest particle size obtained by varying experimental conditions is about 16 nm when using the CN-PPV polymer of high molecular weight (~235 000). These results indicate that the preparation method for different sized particles has to be optimized for each polymer on a case-by-case basis. In present study, we attempt to prepare different-sized Pdots together with controlled chain folding behavior, as revealed by single molecule spectroscopy that the emission profile of conjugated polymers evolves in the size range between single polymer chain and the bulk material.[9]

We choose CN-PPV polymer (MW ~235 000, chemical structure shown in Figure 1a) because this type of Pdots exhibit high fluorescence quantum yield (~50%).[30] To obtain CN-PPV Pdots of different size, we employed a two-step reprecipitation strategy modified from previous reports.[28] First, the polymer precursor solution was completely dissolved in THF, but further diluted in THF containing certain volume fractions of water. Presumably, the slight decrease in solvent quality may lead to the formation of small polymer aggregates with relatively extended chain conformation in the solution. Further mixing this solution with water can produce polymer nanoparticles with relative large sizes and maintain their extended chain conformation. Indeed, CN-PPV nanoparticles of three different sizes were prepared by using the two-step reprecipitation approach. As indicated by DLS measurements (Figure 1b), an average particle size of 16 nm was determined for the CN-PPV Pdots prepared from the polymer (MW ~235 000) in pure THF solution. With the same experimental conditions but increasing water fraction in the polymer precursor solutions, the resulting Pdots show increased particle size, ~33 nm for those prepared from polymer in THF/water (2:1) and ~59 nm for THF/water (1:1), respectively. While there are batch-to-batch variations in some cases, a general trend observed in our experiments is that the particle size is increased with increasing the water content in the precursor solution. These results indicate the Pdot size can be successfully tuned by adjusting the precursor solvent quality. For the

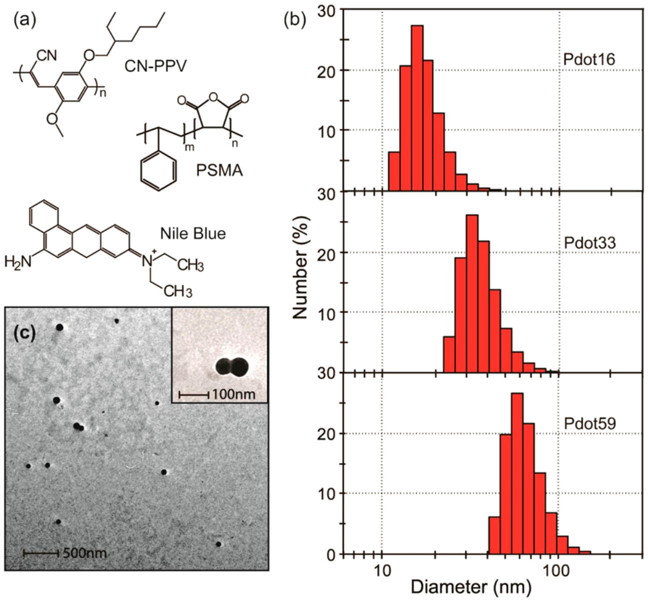

Figure 1. (a) Chemical structure of semiconducting polymer CV-PPV and Nile blue dye. (b) Dynamic light scattering (DLS) results of the semiconducting polymer dots obtained by the two-step repreciptation method. The top, middle, and bottom show the DLS data of Pdot16, Pdot33, and Pdot59, respectively. (c) Typical transmission electron microscopy (TEM) image of Pdot59. A magnified image is shown in the inset.

convenience in our discussion, these nanoparticles are abbreviated as Pdot16 for 16 nm diameter nanoparticles, Pdot33 for 33 nm diameter nanoparticles, and Pdot59 for 59 nm diameter nanoparticles, respectively. The particle size and morphology were further characterized by transmission electron microscopy (TEM). The Pdot59 nanoparticles were drop-cast onto copper grids and a representative TEM image is shown in Figure 1c. The TEM image show comparable particle size and distribution in that the lateral size of the collapsed particle from TEM is largely consistent with the hydrodynamic size from DLS.[31] The TEM image also indicate spherical morphology of the CN-PPV particles, in good agreement with the previously reported observation that the equilibrium shape for conjugated polymer nanoparticles tends to be spherical because surface tension effects determine the morphology in this size range.[32]

Polymer Conformation and Spectroscopy. Conjugated polymers are characterized as rigid rodlike polymers due to the rigidity of the π-conjugated backbone. The real polymer conformation in solution and films, however, do not have the ideal extended structures because they tend to twist and coil. An intuitive description of a conjugated polymer chain is that of a series of linked chromophores, each of which has a different extent of π-electron delocalization. The longer segments have lower $\pi-\pi^*$ energy gaps according to a 1D particle-in-a-box picture of electron delocalization along these segments. As a result, the absorption spectrum of a conjugated polymer consists of an inhomogeneous superposition of absorptions from segments with different conjugation lengths. In contrast, the emission spectrum is highly Stokes-shifted because excitons on high-energy segments will undergo rapid energy transfer to lower-energy segments, so that nearly all the emission comes from low energy, long conjugation length chromophores. In densely packed polymer films and nanoparticles, the presence of chain defects as well as interchain interactions result in complex polymer conformation, which has a large impact on the optical and electronic properties of the polymer. As demonstrated in previous reports,[6−8] the degree of interchain interactions and morphology in conjugated polymer films can be controlled by varying the solvent and polymer concentration of the solution from which the films are cast. These studies led us to ask whether the strategy can be used to tailor the optical properties of conjugated polymer nanoparticles.

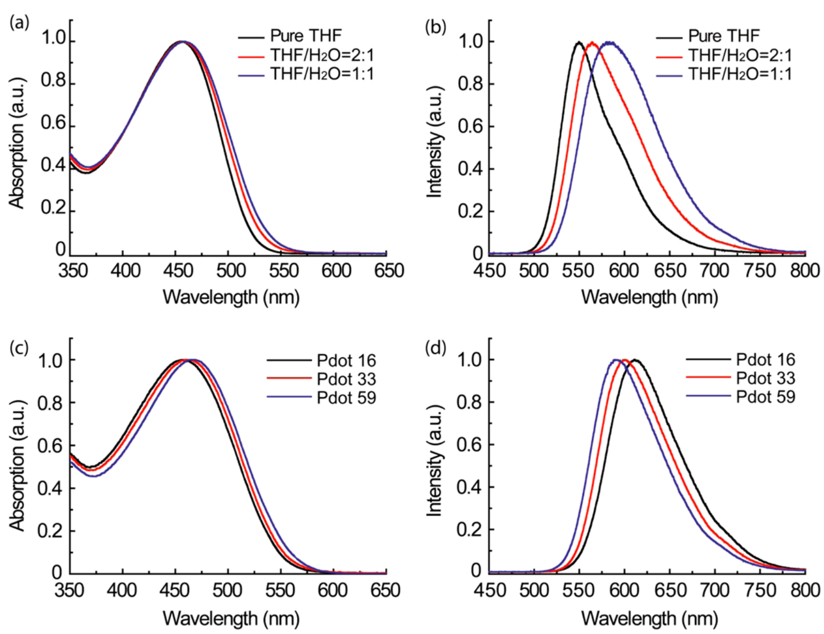

Figure 2. Absorption and fluorescence spectroscopy of CN-PPV polymer in solution phase and nanoparticle form. (a, b) Absorption and emission spectra of the polymer in THF solutions containing different fractions of water. (c, d) Absorption and emission spectra of the Pdots with different sizes obtained by varying the precursor solvent quality.

We demonstrate the polymer conformation and spectroscopic properties of Pdots can be controlled by altering the chain conformation in the solution from which the nanoparticles are prepared. In a good solvent such as THF, the CN-PPV polymer adopts a relatively open and straight conformation, which is best to maximize the solvent−solute interactions. With gradually decreasing the solvent quality by adding water to the solution, the polymer chains may curl up to a much tighter coil or form chain−chain aggregates, depending on the polymer concentration. This change in conformation can be identified by spectroscopy as the tight coil usually exhibits blue-shifted absorption and emission due to decreased conjugation length while both spectra of chain aggregates are red-shifted because of increased interchain interactions. Panels a and b in Figure 2 show the absorption and emission spectra of the CN-PPV in THF solutions containing different fractions of water. With increasing the water content in the solution, the absorption spectra of the CN-PPV polymer are slightly red-shifted and broadened, accompanied by an apparent appearance of red tail. This observation is a characteristic of the formation of interchain aggregation rather than self-aggregation caused by coiling. The increased interchain interactions are also reflected by the emission spectra which show a clear red-shift as the water content is increased (Figure 2b). The red shift in both absorption and emission spectra indicate the polymer molecules form chain−chain aggregates in the precursor solutions by the addition of water.

Pdots of variable sizes were accordingly obtained by rapid mixing the above precursor solutions with water. Fluorescence spectroscopy indicates that the polymer conformation in solution phase largely affects the polymer folding and packing during the nanoparticle preparation process, resulting in solution-phase control over the morphology and photophysics of semiconducting polymer nanoparticles. Panels c and d in Figure 2 show the absorption and emission spectra of the Pdot16, Pdot33, and Pdot59, respectively. It is apparent that smaller Pdots show blue-shifted absorption and red-shifted emission as compared to the larger particles. We believe this trend is closely related to the polymer conformation in the precursor solutions. Presumably, the polymer molecules in pure THF experience the largest drop of solvent quality during nanoparticle preparation, resulting in more kinking and bending of polymer backbones. Consequently, this preparation yielded small particles with densely packed chromophores. The observed blue-shift in absorption for Pdot16 is consistent with an overall decrease in the conjugation length and the red-shift in emission agrees well with the strong interchain interactions. In contrast, chain−chain aggregates were preformed in the THF/water mixtures, and the memory of this solution phase conformation was largely retained during nanoparticle preparation because of the mild change in solvent quality as compared to the preparation using pure THF. As a result, the emission spectrum of Pdot59 particles is similar to that of their precursor solution, whereas Pdot33 and Pdot16 exhibit apparent red-shifts in emission spectra (Figure 2b and 2d). It is worth noting that Pdot16 show emission peak centered 610 nm, a red-shift of ~20 nm from that of Pdot59. Fluorescence quantum yield measurements indicate the Pdot16 show a slightly decreased quantum yield (~42%) as compared to that of Pdot59 (~49%). These results suggest that highly fluorescent Pdots of tunable emission colors can be obtained for the semiconducting polymer CN-PPV by tailoring the preparation conditions.

Size-Dependent Single-Particle Brightness. Selection of appropriate particle size is particularly important for single-particle tracking and imaging applications. However, the brightness-size relationship has not been experimentally explored for semiconducting polymer nanoparticles. The fluorescence brightness is generally estimated by the product of the per-particle absorption cross section and the fluorescence quantum yield. Bulk spectroscopic measurements indicate that three types of Pdots have comparable fluorescent quantum yield (~40−50%), therefore the per-particle brightness is primarily determined by the absorption cross-section. Assuming the same packing density for the polymer chromophores, the number of chromophores in a particle is scaled with the particle volume. Thus, the absorption cross section is expected to follow a cubic dependence on the particle diameter, i.e., a 2-fold increase in particle diameter would yield an 8-fold increase in absorption cross-section. On the basis of the above estimation, the single-particle brightness of Pdot33 is estimated to be ~8.8 times brighter than that of Pdot16. However, the actual brightness difference is likely deviated from this estimation and a side-by-side brightness comparison should provide a useful reference.

We performed single-particle brightness measurements to compare the actual brightness with those estimated from bulk spectroscopy and particle size. First, we measured the single-particle fluorescence brightness of Pdot33 and Pdot16, respectively. Fluorescence imaging of the two types of Pdots was conducted on a TIRF microscope under identical excitation and detection conditions (Figure 3a, b). As shown by the fluorescence images, Pdot33 exhibited an obvious improvement in signal-to-background ratio compared to Pdot16. This improvement is primarily due to the high per-particle absorption cross section of large sized Pdots. Intensity histograms were obtained by statistical analyses of hundreds of particles in single-particle images. As indicated by the intensity histograms (Figure 3d and 3e), the measured average fluorescence brightness of Pdot33 is about 3.6 times higher than that of Pdot16. This value is much lower than the estimated ratio (8.8 times) based on the particle size.

Single particle imaging indicates the majority of Pdot59 particles saturated the CCD detector under the same experimental conditions for Pdot16 and Pdot33. To make reliable measurements, we perform single particle imaging on Pdot33 and Pdot59 by using low excitation power. After statistical analysis, the brightness intensities of Pdot59 were back-calculated according to the fluorescence intensity ratio of Pdot33 under the two excitation densities. In this way, the per-particle brightness of the three types of Pdots can be compared directly by the intensity histogram (Figure 3d-3f). As seen from the Figure, Pdot59 nanoparticles are 3.4 times brighter than Pdot33, and 12.8 times brighter than Pdot16, primarily following a quadratic dependence on the particle size. The experimentally determined brightness ratio is deviated from those estimated by considering a cubic dependence of brightness on particle size. The discrepancy can be attributable to the excitation profile of the TIRF microscope. Because the excitation in a TIRF microscope is due to the evanescent field, which decays exponentially as a function of the distance from the coverslip surface, the excitation for large particles is not as effective as that for small particles. Other reasons may also contribute to the discrepancy, for example, the DLS measurement is generally biased for large nanoparticles, therefore the obtained particle sizes may be deviated from the actual size

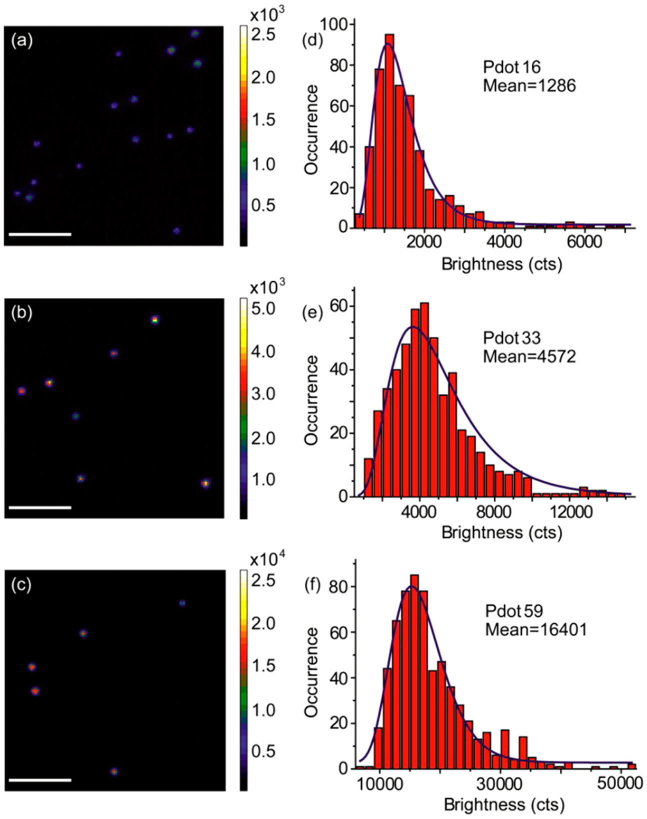

Figure 3. Size -dependent single-particle brightness of different-sized Pdots. (a−c) Single-particle fluorescence images of Pdot16, Pdot33, and Pdot59, respectively, obtained under identical excitation and detection conditions. (d−f) Intensity histograms by analyzing single-particle brightness of hundreds of nanoparticles. The blue curves were obtained by fitting a log-normal distribution to the histogram, resulting in average intensities of 1286, 4573, and 16401 counts for the three types of Pdots, respectively. Scale bar represents 5 μm.

distributions. In addition, the particle size determined by DLS is hydrated diameter, and the hydration of these hydrophobic Pdots may vary upon size change. Nevertheless, the single-particle imaging experiments reveal that 2-fold increase in particle diameter yield at least 4-fold increase in fluorescence brightness for the CN-PPV Pdots. As Pdots exhibit exceptional tracking uncertainty (∼1 nm) for single particle tracking,[33] this information is useful for considering the size effect for a broad range of particle tracking and imaging applications.

Size-Dependent Fluorescence Quenching. We choose CN-PPV Pdots as donor and Nile blue dye as acceptor to investigate the size-dependent quenching and energy transfer from the nanoparticle to the surface-adsorbed dye. Zeta potential measurements show that the bare CN-PPV Pdots have a negatively charged surface with a zeta potential of −40 mV. For the three types of Pdots, PSMA functionalization results in an increase of the surface charge to approximately −55 mV, with little dependence on the particle size. The highly charged Pdots can complex with the oppositely charged molecules through electrostatic interactions, a requirement for efficient quenching in many conjugated polyelectrolytes via the amplified energy transfer. As shown by the spectral overlap (see the Supporting Information, Figure 1), efficient energy transfer via Förster mechanism is highly possible. Indeed, fluorescence quenching was observed in CN-PPV nanoparticles mixed with a small fraction of Nile blue dye (1 wt % relative to the Pdots). The normalized absorption spectra, fluorescence excitation and emission spectra of Pdot16 nanoparticles mixed with 1 wt % Nile blue dye support the fact that the Pdots and dye molecules form stable Pdot-dye complex driven by electrostatic interactions between the negatively charged Pdots and positively charged dye molecules (see the Supporting Information, Figure 2).

Highly efficient energy transfer is evident in the evolution of the fluorescence spectra with increasing dye concentration. Figure 4a shows the absorption spectra of the Pdot16 solution containing varying concentrations of Nile blue dye. The

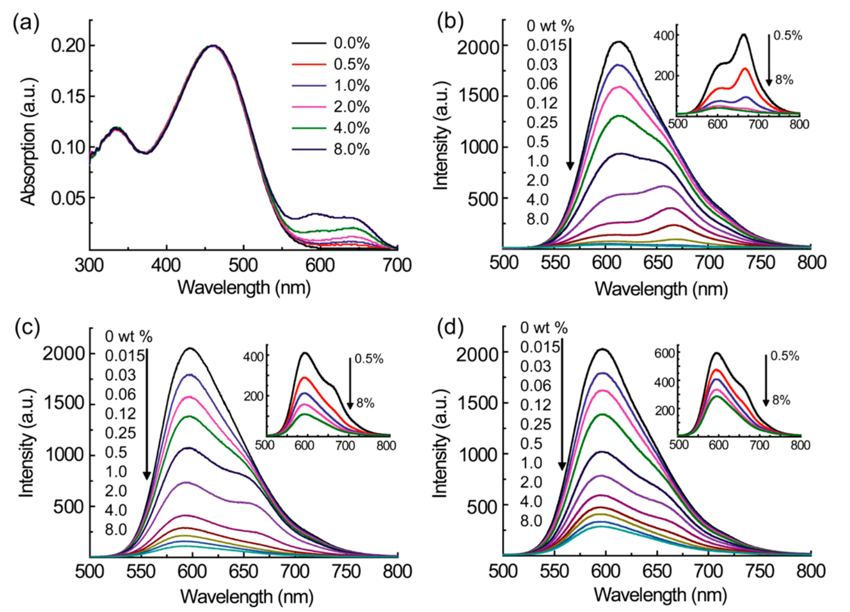

Figure 4. Fluorescence quenching of CN-PPV Pdots by surfaced adsorbed dye molecules. (a) Absorption spectra of the Pdots in the presence of Nile blue dye at different concentrations. (b−d) Fluorescence emission spectra of the Pdots with increasing the Nile blue concentration. Smaller Pdots such as (b) Pdot16 show higher quenching efficiency as compared larger particles such as (c) Pdot33 and (d) Pdot59.

absorption profile from the CN-PPV Pdots remains almost constant and the absorption peak of fluorescence dye molecule is increased with increasing dye content. Figure 4b−d shows the fluorescence emission spectra of the three types of CN-PPV nanoparticles mixed with Nile blue dye of varying concentrations. As exemplified by the Pdot16 particles (Figure 4b), the fluorescence from the Pdots decreases with increasing dye content, whereas fluorescence from the dye appears and becomes evident at the dye concentration around 0.5 wt %. As the dye concentration is increased from 0.5 to 8 wt %, the fluorescence of Pdot16 nanoparticles is greatly quenched. The emission intensity of the dye also drops at this concentration range, consistent with the formation of dye aggregates with low fluorescence quantum yield. When the dye concentration is greater than 4 wt %, both the Pdot16 and the dye are completely quenched, with negligible fluorescence observed from the solution. The Pdot33 and Pdot59 show similar trends in the evolution of the fluorescence as the fraction of the dye is increased (Figure 4c, d). At the dye concentration of 0.12 wt %, both the two types of nanoparticles were quenched by ∼50%, comparable to that of Pdot16. However, at high dye concentration, the quenching efficiency of both Pdot33 and Pdot59 was apparently lower than that of Pdot16. For example, at the final dye concentration of 8 wt %, the fluorescence intensities of Pdot33 and Pdot59 were quenched to 5% and 14% of the emission intensity in absence of the dye, respectively. These values are higher than that of the Pdot16 (∼2%), indicating that the quenching efficiency is decreased with increasing the particle size.

The size-dependent quenching efficiency can be explained by an intuitive description based on quenching volume. Considering a system without energy migration, i.e. the quenching occurred by one-step Förster energy transfer, the quenching volume would be determined by the Förster radius, which is calculated to be ∼6.0 nm for the Pdot16 and Nile blue dye according to their spectral overlap. Calculation using the spectral overlap and quantum yields of Pdot33 and Pdot59 as donors show little change as compared to Pdot16, and similar Förster radii were obtained for the two types of larger particles, 6.0 nm for Pdot33 and 5.9 nm for Pdot59, respectively. However, excitons in semiconducting polymers can migrate along the polymer chain and hop between chains, processes characterized by an exciton diffusion length, typically on the order of 5−6 nm for various PPV derivatives.[34] The exciton diffusion can result in an effective energy transfer distance that is larger than Förster radius, for example, by a factor of 15−20% for an exciton diffusion length of 8 nm.[21] According to these values, the effective energy transfer distances in the three types of Pdots are approximately the same and estimated to be ∼7 nm. For a dye molecule located at the particle surface, the quenching volume equals to the intersected volume between the particle sphere and that defined by the effective energy transfer distance. At low dye concentrations, the quenching efficiencies in the three types of Pdots are comparable because the dye molecules are sparsely adsorbed on the surface and quench similar numbers of fluorophores in the quenching volume. With increasing the dye concentration, the Pdot surface may be covered by a monolayer of dye molecules. At this stage, the quenching volume approaches a constant, dependent on the nanoparticle size. Small particles such as Pdot16 were completely quenched because their size is comparable to the effective energy transfer distance. However, Pdot33 and Pdot59 were not completely quenched, as the peripheral layer of these larger particles can be quenched, but fluorophores in their cores remain fluorescent. In the high concentration range, the Pdot surface can be fully covered, with a portion of dye molecules free-floating in solution. In addition, the surface to volume ratio may also contribute to the size-dependent quenching, as smaller particles tend to adsorb more dye molecules for a given Pdot weight concentration.

Quenching Mechanism by Stern−Volmer Analysis and Time-Resolved Study. Fluorescence quenching can be described by two primary mechanisms, static and dynamic quenching, respectively.[35] The former results from the formation of a nonfluorescent ground-state complex, while the latter occurs as a result of diffusive encounters between the fluorophore and quencher during the lifetime of the excited state. For a pure static or dynamic pathway, the quenching can be modeled using the Stern−Volmer relation, which can be expressed as[35]

$$F_0/F = 1 + K_{SV}[Q]$$

where F_0 and F are fluorescence intensities in the absence and presence of quencher, respectively. K_{SV} is the Stern−Volmer quenching constant, and $[Q]$ is the concentration of the quencher. In the case of dynamic quenching, $K_{SV} = k_q\tau_0$, where k_q is the biomolecular quenching constant and τ_0 is the fluorescence lifetime of the fluorophore in absence of the quencher. In the case of static quenching, K_{SV} equals to the binding constant of the nonfluorescent ground-state complex.

Figure 5a presents the Stern−Volmer quenching plots for the three types of Pdots by Nile blue dye in the entire concentration range. Again, these plots exhibit apparent size dependent behavior, and they all deviate from the linear

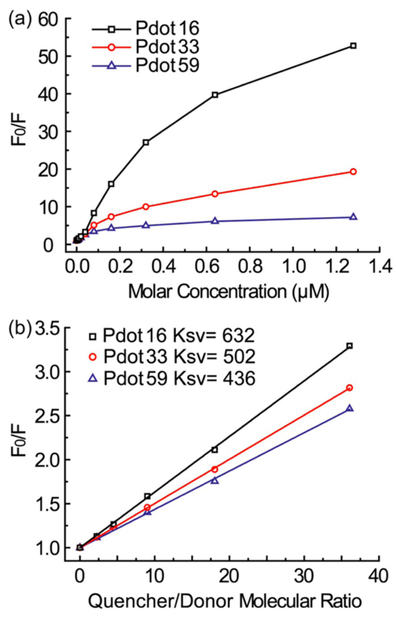

Figure 5. (a) Fluorescence quenching of different-sized Pdots by Nile blue dye. The downward curvatures at high concentrations indicate higher quenching efficiency for smaller particles. (b) Stern−Volmer plots of the fluorescence quenching versus the molar ratio of quencher to polymer repeating unit (PRU). The scattered points are experimental results and the solid lines represent fits to the Stern−Volmer equation. The obtained K_{sv} values show each dye acceptor can quench 400−600 PRUs, indicating highly efficient quenching of Pdots by single dye molecules.

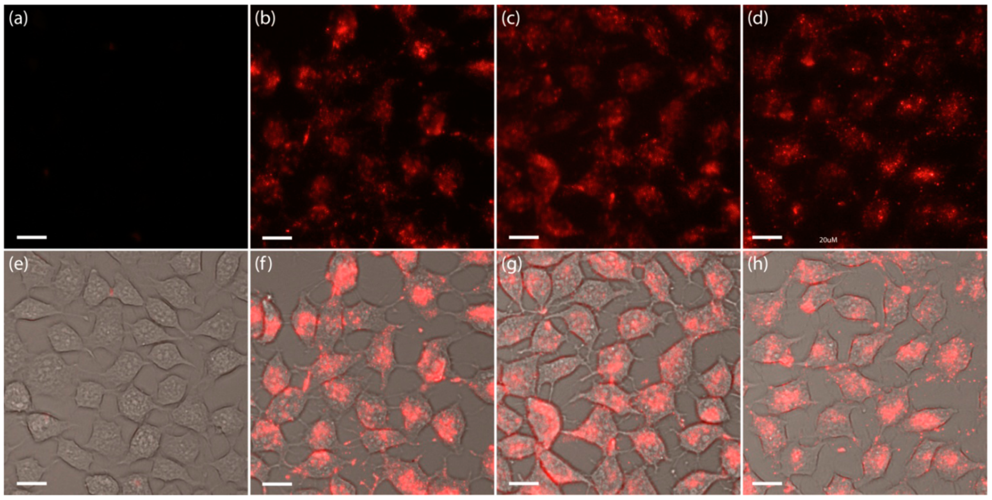

Figure 6. Fluorescence imaging of human breast cancer cells incubated with different sized Pdots. (a) Control samples where the cells were incubated in absence of Pdots. (b−d) Fluorescence images of live MCF-7 cells incubated with (b) Pdot16, (c) Pdot33, and (d) Pdot59, respectively. (e−h) Combined bright-field and fluorescence image. Scale bar represents 20 μm.

relationship with downward curvatures toward the [Q] axis at high concentrations (>0.16 μM, 1 wt %). This deviation is indicative of the presence of two quencher populations and one population is not bound to the Pdots. Careful examinations of the Stern−Volmer plots indicate that the quenching of Pdot16 is clearly curved upward around 0.04 μM (0.25 wt %). As Stern−Volmer plot of F_0/F vs [Q] is linear for a purely static or dynamic pathway, upward curvature is generally a characteristic feature of the occurrence of mixed static and dynamic quenching.[35] To provide a quantitative measure of the quenching efficiency, we discuss the quenching at low quencher concentrations where the plots are nearly linear. K_{SV} values obtained by linear fittings are 3.9×10^7 M^{-1} for Pdot59, 4.5×10^7 M^{-1} for Pdot33, and 5.7×10^7 M^{-1} for Pdot16, respectively. These values are comparable or higher than those determined in the amplified quenching of various conjugated polyelectrolytes by small molecule such as methyl viologen, cyanine and rhodamine dyes.[12,36,37] The further increased quenching efficiency is perhaps due to the enhanced exciton diffusion distance in polymer nanopartilcles as compared to the one-dimensional migration in polyelectrolytes. K_{SV} values sometimes depend on polymer concentration, meanwhile molecular weights of polymer molecules are generally polydisperse and can vary from batch to batch. We use the ratio of quencher to polymer repeating unit (PRU) to avoid this difficulty. If the quencher concentration is expressed as a molecule fraction of $[Q]/[PRU]$, K_{sv} represents the number of polymer repeating units quenched by a single quencher. Fitting of the Stern−Volmer plots (Figure 5b) indicated that approximately 436−632 PRUs are quenched by single dye molecules. Considering that the fluorophores are densely packed with a density of ∼1 g/cm^3,[28] the PRU number quenched by single dye is consistent with the quenching volume by intersecting the particle volume with the effective energy transfer distance (∼7 nm). Taken together, these results indicate surface dye molecules can quench Pdots with efficiencies comparable or higher than polyelectrolytes and suggest that Pdots are promising platforms for energy transfer-based sensors or molecular beacons.

Stern−Volmer analysis also provides insight into the mechanism for the amplified quenching in the Pdots. When the quenching is fully dynamic, K_{SV} is determined by the product of diffusion rate constant k_q (typically <1 × 10^{10} M^{-1} s^{-1}) and fluorescence lifetime τ_0 (∼2.2 ns for CN-PPV Pdots). This places an upper limit on K_{SV}(∼20 M^{-1}). The experimentally observed K_{SV} values for Pdot quenching are significantly larger than 20 M^{-1}, which cannot be accounted for by a diffusion-controlled process. Association of the cationic dye quenchers with the anionic Pdots must be involved in the quenching mechanism. Static quenching can be further confirmed by time-resolved studies. As static quenching results from the formation of nonfluorescent complex, the fluorescence is only from the uncomplexed fraction, and hence the fluorescence lifetime remains unchanged. In contrast, for dynamic quenching $F_0/F = \tau_0/\tau$. The fluorescence decays of the Pdot16 mixed with different dye concentrations are measured by a time-correlated single-photon counting instrument (TCSPC, see the Supporting Information, Figure 3). At low dye concentration such as 0.01 μM (0.06 wt %), where $F_0/F = 1.6$, the fluorescence lifetime was nearly identical with that in absence of the dye (∼2.2 ns), indicating static quenching is a dominant pathway at low concentrations. As further increasing the dye concentration, dynamic processes make contribution to the overall quenching, as indicated by the fluorescence lifetime decreases to ∼1.2 ns for the Pdot solution containing 0.08 μM dye (0.5 wt %, $F_0/F = 8.3$), and ∼0.4 ns for the solution containing 1.28 μM dye (8 wt %, $F_0/F = 52.8$).

Picosecond time-resolved fluorescence experiments were performed to explore the energy transfer mechanism from the Pdots to Nile blue dye. By using a laser excitation wavelength of 400 nm, where the absorption of Nile blue is minimal, fluorescence from the surface dye (inset of Figure 4b) is created almost exclusively by energy transfer from the polymer with concomitant quenching of the Pdots. Figure 4 in the Supporting Information shows the fluorescence decay detected at 610 nm with 400 nm excitation for Pdot-dye solutions parallel to the TCSPC measurements. As shown in the figure, the picosecond-resolved decay curve for 0.01 μM dye concentration (0.06 wt %) remains the same to that of the pure Pdot solution, whereas those at higher dye concentrations decays more rapidly. Steady-state spectroscopy indicates the Pdot fluorescence was quenched considerably (∼38%) by

dx.doi.org/10.1021/am502733n | ACS Appl. Mater. Interfaces 2014, 6, 10802−10812

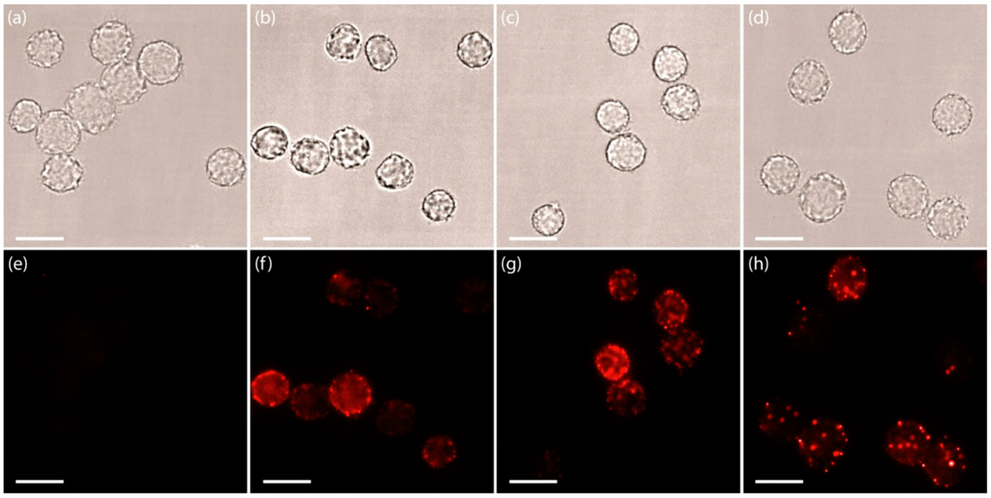

Figure 7. Fluorescence imaging of cell surface marker (EpCAM) in human breast cancer cells labeled with Pdot-steptavidin bioconjugates. MCF-7 cells were incubated sequentially with biotinylated primary anti-EpCAM antibody and different sized Pdot-streptavidin bioconjugates. (a−d) Bright-field images and (e−h) fluorescence images. (e) Control samples where the cells were incubated in absence of primary antibody. (f−h) Fluorescence images of MCF-7 cells incubated with primary antibody and streptavidin conjugates of (b) Pdot16, (c) Pdot33, and (d) Pdot59, respectively. Scale bar represents 20 μm.

energy transfer at 0.01 μM dye concentration (0.06 wt %, Figure 4b). Taken together, these results reveal that the Pdot-to-dye energy transfer takes place on two distinct time scales. A significant fraction of the excitation energy was transferred to surface dye through a pathway that is too fast to be resolved within the instrument response (∼400 fs), while a slower energy transfer pathway is present at higher dye concentrations, as evidenced by the noticeable increase in their decay rates (see the Supporting Information, Figure 4). Similar decay kinetics was previously observed in fluorescence quenching of conjugated polyelectrolyte by cationic cyanine dyes.[37,38] As suggested in early reports,[37] the fast quenching pathway was attributed to prompt quenching of excitons produced in the dark region of a bound dye, whereas the slower quenching pathway was proposed to be due to diffusion of excitons to the quenching sites. In addition, diffusional quenching by free acceptors in solution also becomes important at high dye concentrations.

Size Dependent Cellular Labeling. The three types of Pdots were employed to investigate the effect of nanoparticle size on cellular uptake in cultured mammalian cells. This study was stimulated by novel applications in biomedicine where Pdots have been used to achieve drug delivery and photo-dynamic therapy.[39,40] We attempt to address an important question to the realization of Pdot-based therapeutic agents, namely, what is the optimal particle size for optimal endocytosis. As weight concentration is generally adopted for drug delivery, we use the same weight concentration of Pdot (∼25 ppm) to incubate with MCF-7 cells for 24 h. Fluorescence imaging (Figure 6) showed obvious Pdot internalization after 24h incubation with the nanoparticles (Pdots16, Pdots33, and Pdots59), as compare with the control group (without Pdots). These images indicate a staining pattern consistent with perinuclear labeling and brightly fluorescent vacuoles and organelles (e.g., pinosomes and lysosomes). The mechanism of cellular uptake of these fluorescent Pdots have been systematically investigated in a previous report,[41] in which temperature-dependent uptake, colocalization study, and inhibition of uptake by phosphoinositide 3-kinase inhibitors indicated macropinocytosis as the operative endocytic mechanism. To quantify the size-dependent cellular uptake, we performed flow cytometry to analyze the fluorescence intensity of these cells. As shown by the flow results (Figure 8a), the maximum fluorescence intensity relative to the control was observed for Pdot33, which indicates cellular uptake of the medium-size Pdots is more effective than those of Pdot16 and Pdot59 particles. The difference in cellular uptake is likely due to the combined effect of several factors such as the surface charge, functionalization, and surface-to-volume ratio related to particle diameters.

We further investigate the size effect in specific labeling using biotin−streptavidin interactions. The PSMA functionalization generate surface carboxyl groups so that streptavidin can be covalently conjugated to the different sized Pdots by a protocol described before.[31] The Pdot bioconjugates were used to label a specific celllular target, EpCAM, an epithelial cell-surface marker currently used for the detection of circulating tumor cells. A biotinylated primary anti-EpCAM antibody and the Pdot-streptavidin probes were sequentially incubated with MCF-7 cells. Figure 7 shows fluorescence images of the labeling cells as well as the control sample. Strong fluorescence was observed on the cell surface compared to the control sample (identical conditions but without the primary antibody), indicating all the Pdot-streptavidin (Pdots16, Pdots33, and Pdots59) were highly specific for the target. It is worth noting that the labeling pattern is also dependent on the particle size. The small Pdot probes show a relatively uniform surface labeling, whereas the large probes such as Pdot59 exhibit bright clusters on cell surfaces. Steric hindrance due to the large particle size is likely responsible for the different labeling patterns. The labeling brightness of the three types of Pdot-streptavidin probes was quantified using flow cytometry. As shown in Figure 8b, the fluorescence intensity of Pdot-labeled cells were clearly separated from the background, and shifted to high intensity with decreasing the Pdot size, indicating that small-sized Pdots are more efficient for cell-surface labeling than the large Pdot-bioconjugates. The size dependent cell-labeling brightness suggests appropriate particle size should be selected for using the Pdot probes in biological applications.

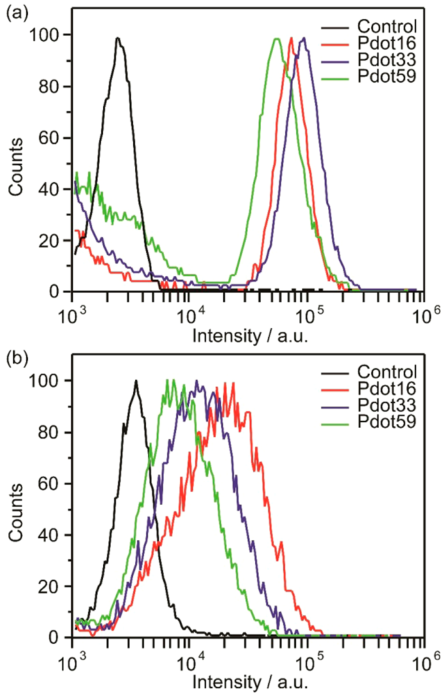

Figure 8. Flow cytometry analysis of cellular uptake and labeling brightness. (a) Fluorescence intensity distributions of live MCF-7 cells incubated with different sized Pdots. (b) Fluorescence intensity distributions of MCF-7 cells labeled with primary anti-EpCAM antibody and Pdot-streptavidin bioconjugates.

CONCLUSION

We prepared fluorescent polymer dots of different sizes and investigated the size effect on their fluorescence properties. The polymer conformation in solution phase largely affects the polymer folding and packing during the nanoparticle preparation, resulting in the controlled chain-packing behavior and photophysics of semiconducting polymer nanoparticles. The resulting Pdots exhibit apparent size dependent absorption and emission, consistent with the polymer conformation due to different preparation conditions. We employ single-particle fluorescence imaging to perform a side-by-side comparison on the Pdot brightness. Quantitative analysis and statistics on single particle imaging data indicate a quadratic dependence of single-particle brightness on particle size. Upon introducing a positively charged dye Nile blue, the Pdots were quenched very efficiently ($K_{sv} > 1 \times 10^7$ M^{-1}) by energy transfer to the cationic surface dye in an applied quenching process. Steady-state and time-resolved spectroscopy indicate that the efficient quenching occurs primarily via static pathway due to the formation of electrostatic nanoparticle-dye complex. The three types of Pdots were used for cell uptake and cellular labeling involving biotin−streptavidin interactions. Fluorescence imaging and with flow cytometry studies clearly show that medium-sized Pdots exhibit the highest uptake efficiency, whereas small-sized Pdots are more effective for immunefluorescent labeling of cell surface. These results emphasize that selecting an appropriate particle size is significant for using Pdot probes in fluorescence imaging and sensing applications.

ASSOCIATED CONTENT

Supporting Information

Fluorescence spectra of Pdots and nile blue dye, fluorescence lifetimes of Pdots quenched by nile blue dye at different concentrations. This material is available free of charge via the Internet at http://pubs.acs.org.

AUTHOR INFORMATION

Corresponding Authors

*E-mail: cwu@jlu.edu.cn. Phone: +86-431-8515-3853. Fax: +86-431-8516-8270.
*E-mail: wpqin@jlu.edu.cn.

Notes

The authors declare no competing financial interest.

ACKNOWLEDGMENTS

C.W. acknowledges financial support from “Thousand Young Talents Program” and the National Science Foundation of China (Grants 61222508 and 61335001). This work is also supported by the Key Laboratory of Optoelectronic Devices and Systems of Ministry of Education and Guangdong Province.

REFERENCES

(1) Wu, C.; Bull, B.; Szymanski, C.; Christensen, K.; McNeill, J. Multicolor Conjugated Polymer Dots for Biological Fluorescence Imaging. *ACS Nano* **2008**, *2*, 2415−2423.
(2) Wu, C.; Chiu, D. T. Highly Fluorescent Semiconducting Polymer Dots for Biology and Medicine. *Angew. Chem., Int. Ed.* **2013**, *52*, 3086−3109.
(3) Pecher, J.; Mecking, S. Nanoparticles of Conjugated Polymers. *Chem. Rev.* **2010**, *110*, 6260−6279.
(4) Zhu, C. L.; Liu, L. B.; Yang, Q.; Lv, F. T.; Wang, S. Water-Soluble Conjugated Polymers for Imaging, Diagnosis, and Therapy. *Chem. Rev.* **2012**, *112*, 4687−4735.
(5) Kaeser, A.; Schenning, A. P. H. J. Fluorescent Nanoparticles Based on Self-Assembled π-Conjugated Systems. *Adv. Mater.* **2010**, *22*, 2985−2997.
(6) Nguyen, T. Q.; Doan, V.; Schwartz, B. J. Conjugated Polymer Aggregates in Solution: Control of Interchain Interactions. *J. Chem. Phys.* **1999**, *110*, 4068−4078.
(7) Nguyen, T.-Q.; Martini, I. B.; Liu, J.; Schwartz, B. J. Controlling Interchain Interactions in Conjugated Polymers: The Effects of Chain Morphology on Exciton−Exciton Annihilation and Aggregation in MEH−PPV Films. *J. Phys. Chem. B* **2000**, *104*, 237−255.
(8) Schwartz, B. J. Conjugated Polymers as Molecular Materials: How Chain Conformation and Film Morphology Influence Energy Transfer and Interchain Interactions. *Annu. Rev. Phys. Chem.* **2003**, *54*, 141−172.
(9) Grey, J. K.; Kim, D. Y.; Norris, B. C.; Miller, W. L.; Barbara, P. F. Size Dependent Spectroscopic Properties of Conjugated Polymer Nanoparticles. *J. Phys. Chem. B* **2006**, *110*, 25568−25572.
(10) Gaab, K. M.; Bardeen, C. J. Wavelength and Temperature Dependence of the Femtosecond Pump−Probe Anisotropies in the Conjugated Polymer MEH-PPV: Implications for Energy-Transfer Dynamics. *J. Phys. Chem. B* **2004**, *108*, 4619−4626.
(11) Wang, F.; Han, M.-Y.; Mya, K. Y.; Wang, Y.; Lai, Y.-H. Aggregation-Driven Growth of Size-Tunable Organic Nanoparticles Using Electronically Altered Conjugated Polymers. *J. Am. Chem. Soc.* **2005**, *127*, 10350−10355.
(12) Chen, L.; McBranch, D. W.; Wang, H. L.; Helgeson, R.; Wudl, F.; Whitten, D. G. Highly Sensitive Biological and Chemical Sensors Based on Reversible Fluorescence Quenching in a Conjugated Polymer. *Proc. Natl. Acad. Sci. U.S.A.* **1999**, *96*, 12287−12292.
(13) Fan, C.; Plaxco, K. W.; Heeger, A. Electrochemical Interrogation of Conformational Changes as a Reagentless Method for the

Sequence-Specific Detection of DNA. *Proc. Natl. Acad. Sci. U.S.A.* **2003**, *100*, 9134−9137.

(14) Pinto, M. R.; Schanze, K. S. Amplified Fluorescence Sensing of Protease Activity with Conjugated Polyelectrolytes. *Proc. Natl. Acad. Sci. U.S.A.* **2004**, *101*, 7505−7510.

(15) McQuade, D. T.; Pullen, A. E.; Swager, T. M. Conjugated Polymer-Based Chemical Sensors. *Chem. Rev.* **2000**, *100*, 2537−2574.

(16) Thomas, S. W.; Joly, G. D.; Swager, T. M. Chemical Sensors Based on Amplifying Fluorescent Conjugated Polymers. *Chem. Rev.* **2007**, *107*, 1339−1386.

(17) Feng, X. L.; Liu, L. B.; Wang, S.; Zhu, D. B. Water-Soluble Fluorescent Conjugated Polymers and Their Interactions with Biomacromolecules for Sensitive Biosensors. *Chem. Soc. Rev.* **2010**, *39*, 2411−2419.

(18) Pu, K. Y.; Liu, B. Fluorescent Conjugated Polyelectrolytes for Bioimaging. *Adv. Funct. Mater.* **2011**, *21*, 3408−3423.

(19) Duarte, A.; Pu, K. Y.; Liu, B.; Bazan, G. C. Recent Advances in Conjugated Polyelectrolytes for Emerging Optoelectronic Applications. *Chem. Mater.* **2011**, *23*, 501−515.

(20) Wu, C.; Peng, H.; Jiang, Y.; McNeill, J. Energy Transfer Mediated Fluorescence from Blended Conjugated Polymer Nanoparticles. *J. Phys. Chem. B* **2006**, *110*, 14148−14154.

(21) Wu, C.; Zheng, Y.; Szymanski, C.; McNeill, J. Energy Transfer in a Nanoscale Multichromophoric System: Fluorescent Dye-Doped Conjugated Polymer Nanoparticles. *J. Phys. Chem. C* **2008**, *112*, 1772−1781.

(22) Wu, C.; Bull, B.; Szymanski, C.; Christensen, K.; McNeill, J. Ratiometric Single-Nanoparticle Oxygen Sensors for Biological Imaging. *Angew. Chem., Int. Ed.* **2009**, *48*, 2741−2745.

(23) Chan, Y. H.; Wu, C.; Ye, F.; Jin, Y.; Smith, P. B.; Chiu, D. T. Development of Ultrabright Semiconducting Polymer Dots for Ratiometric pH Sensing. *Anal. Chem.* **2011**, *83*, 1448−1455.

(24) Ye, F.; Wu, C.; Jin, Y.; Chan, Y. H.; Zhang, X.; Chiu, D. T. Ratiometric Temperature Sensing with Semiconducting Polymer Dots. *J. Am. Chem. Soc.* **2011**, *133*, 8146−8149.

(25) Pu, K.; Shuhendler, A. J.; Rao, J. Semiconducting Polymer Nanoprobe for In Vivo Imaging of Reactive Oxygen and Nitrogen Species. *Angew. Chem., Int. Ed.* **2013**, *52*, 10325−10329.

(26) Lin, Z.; Zhang, G.; Yang, W.; Qiu, B.; Chen, G. CEA Fluorescence Biosensor Based on the FRET between Polymer Dots and Au Nanoparticles. *Chem. Commun.* **2012**, *48*, 9918−9920.

(27) Zhang, C. Y.; Yeh, H. C.; Kuroki, M. T.; Wang, T. H. Single-Quantum-Dot-Based DNA Nanosensor. *Nat. Mater.* **2005**, *4*, 826−831.

(28) Wu, C.; Szymanski, C.; McNeill, J. Preparation and Encapsulation of Highly Fluorescent Conjugated Polymer Nanoparticles. *Langmuir* **2006**, *22*, 2956−2960.

(29) Szymanski, C.; Wu, C.; Hooper, J.; Salazar, M. A.; Perdomo, A.; Dukes, A.; McNeill, J. D. Single Molecule Nanoparticles of the Conjugated Polymer MEH−PPV, Preparation and Characterization by Near-Field Scanning Optical Microscopy. *J. Phys. Chem. B* **2005**, *109*, 8543−8546.

(30) Ye, F.; Wu, C.; Jin, Y.; Wang, M.; Chan, Y.; Yu, J.; Sun, W.; Hayden, S.; Chiu, D. T. A Compact and Highly Fluorescent Orange-Emitting Polymer Dot for Specific Subcellular Imaging. *Chem. Commun.* **2012**, *48*, 1778−1780.

(31) Wu, C.; Schneider, T.; Zeigler, M.; Yu, J.; Schiro, P.; Burnham, D.; McNeill, J.; Chiu, D. T. Bioconjugation of Ultrabright Semiconducting Polymer Dots for Specific Cellular Targeting. *J. Am. Chem. Soc.* **2010**, *132*, 15410−15417.

(32) Yang, Z. Q.; Huck, W. T. S.; Clarke, S. M.; Tajbakhsh, A. R.; Terentjev, E. M. Shape-memory Nanoparticles from Inherently Non-Spherical Polymer Colloids. *Nat. Mater.* **2005**, *4*, 486−490.

(33) Yu, J.; Wu, C.; Sahu, S.; Fernando, L.; Szymanski, C.; McNeill, J. Nanoscale 3D Tracking with Conjugated Polymer Nanoparticles. *J. Am. Chem. Soc.* **2009**, *131*, 18410−18424.

(34) Markov, D. E.; Tanase, C.; Blom, P. W. M.; Wildeman, J. Simultaneous Enhancement of Charge Transport and Exciton Diffusion in Poly(p-phenylenevinylene) Derivatives. *Phys. Rev. B* **2005**, *72*, 045217.

(35) Lakowicz, J. R. *Principles of Fluorescence Spectroscopy*, third ed.; Springer: New York, 2006.

(36) Pinto, M. R.; Kristal, B. M.; K. S, S. A Water-Soluble Poly(phenylene ethynylene) with Pendant Phosphonate Groups: Synthesis, Photophysics, and Layer-by-Layer Self-Assembled Films. *Langmuir* **2003**, *19*, 6523−6533.

(37) Tan, C.; Atas, E.; Müller, J. G.; Pinto, M. R.; Kleiman, V. D.; K. S, S. Amplified Quenching of a Conjugated Polyelectrolyte by Cyanine Dyes. *J. Am. Chem. Soc.* **2004**, *126*, 13685−13694.

(38) Müller, J. G.; Atas, E.; Tan, C.; K. S, S.; V. D, K. The Role of Exciton Hopping and Direct Energy Transfer in the Efficient Quenching of Conjugated Polyelectrolytes. *J. Am. Chem. Soc.* **2006**, *128*, 4007−4016.

(39) Feng, X. L.; Lv, F. T.; Liu, L. B.; Tang, H. W.; Xing, C. F.; Yang, Q.; Wang, S. Conjugated Polymer Nanoparticles for Drug Delivery and Imaging. *ACS Appl. Mater. Interfaces* **2010**, *2*, 2429−2435.

(40) Grimland, J. L.; Wu, C. F.; Ramoutar, R. R.; Brumaghima, J. L.; McNeill, J. Photosensitizer-doped Conjugated Polymer Nanoparticles with High Cross-Sections for One- and Two-photon Excitation. *Nanoscale* **2011**, *3*, 1451−1455.

(41) Fernando, L. P.; Kandel, P. K.; Yu, J.; McNeill, J.; Ackroyd, P. C.; Christensen, K. A. Mechanism of Cellular Uptake of Highly Fluorescent Conjugated Polymer Nanoparticles. *Biomacromolecules* **2010**, *11*, 2675−2682.